Journal of Data Science 21 (4), 715–734
October 2023
DOI: 10.6339/23-JDS1085
Statistical Data Science

Central Posterior Envelopes for Bayesian Functional Principal Component Analysis

Joanna Boland[1], Donatello Telesca[1], Catherine Sugar[1,2,3], Michele Guindani[1], Shafali Jeste[4], Abigail Dickinson[3], Charlotte DiStefano[4], and Damla Şentürk[1,2,*]

[1]*Department of Biostatistics, University of California, Los Angeles, Los Angeles, CA 90025, USA*
[2]*Department of Statistics, University of California, Los Angeles, Los Angeles, CA 90025, USA*
[3]*Department of Psychiatry and Biobehavioral Sciences, University of California, Los Angeles, Los Angeles, CA 90025, USA*
[4]*Division of Neurology, Children's Hospital Los Angeles, Los Angeles, CA 90027, USA*

Abstract

Bayesian methods provide direct uncertainty quantification in functional data analysis applications without reliance on bootstrap techniques. A major tool in functional data applications is the functional principal component analysis which decomposes the data around a common mean function and identifies leading directions of variation. Bayesian functional principal components analysis (BFPCA) provides uncertainty quantification on the estimated functional model components via the posterior samples obtained. We propose central posterior envelopes (CPEs) for BFPCA based on functional depth as a descriptive visualization tool to summarize variation in the posterior samples of the estimated functional model components, contributing to uncertainty quantification in BFPCA. The proposed BFPCA relies on a latent factor model and targets model parameters within a hierarchical modeling framework using modified multiplicative gamma process shrinkage priors on the variance components. Functional depth provides a center-outward order to a sample of functions. We utilize modified band depth and modified volume depth for ordering of a sample of functions and surfaces, respectively, to derive at CPEs of the mean and eigenfunctions within the BFPCA framework. The proposed CPEs are showcased in extensive simulations. Finally, the proposed CPEs are applied to the analysis of a sample of power spectral densities from resting state electroencephalography where they lead to novel insights on diagnostic group differences among children diagnosed with autism spectrum disorder and their typically developing peers across age.

Keywords *electroencephalography; functional data analysis; modified band depth; modified volume depth; uncertainty quantification*

1 Introduction

The literature on functional data analysis (FDA) has seen rapid growth in the past two decades in the analysis of data where the basic unit of measurement is a high-dimensional object such as a curve, surface or an image (Ramsay and Silverman, 2005). The wide spectrum of application areas include neuroscience, engineering, medicine, economics and geosciences. A major tool for

*Corresponding author. Email: dsenturk@ucla.edu.

Received July 5, 2022; Accepted January 13, 2023

dimension reduction is the functional principal component analysis (FPCA) for modeling functional variability in the data in lower dimensions (Wang et al., 2016; Yao et al., 2012; Cardot, 2007). Recent literature on FPCA models complex dependencies among the functional observations that are observed in close proximity with respect to time or space (Chen and Müller, 2012; Greven et al., 2010; Crainiceanu et al., 2009; Di et al., 2009; Hasenstab et al., 2017; Scheffler et al., 2020; Campos et al., 2022; Zipunnikov et al., 2011; Baladandayuthapani et al., 2008; Staicu et al., 2010). Bayesian FPCA (BFPCA) offers uncertainty quantification on the functional model components, including the mean and eigenfunctions, via credible intervals, without the need for bootstrap. Developments are typically based on expansion of the functional observation or the functional model components on a set of basis functions, followed by dimension reduction. Suarez and Ghosal (2017) expanded functional model components on a basis set and modeled the covariance function via an approximate spectral decomposition, while Montagna et al. (2012) proposed a Bayesian latent factor regression model (BLFRM) that expands each functional observation as a linear combination of a high-dimensional basis set and placed a latent factor model on the basis coefficients. Effective basis selection is achieved in the latter approach via the multiplicative gamma process shrinkage (MGPS) prior of Bhattacharya and Dunson (2011) placed on the factor loadings. Traditional data summaries for uncertainty in the Bayesian setting rely on parametric assumptions or the use of pointwise quantiles. Parametric credible intervals employed in Crainiceanu et al. (2007) assume approximate posterior normality to form pointwise or simultaneous credible intervals through estimation of pointwise variation in the posterior sample. Krivobokova et al. (2010) proposed quantile credible intervals using the estimated posterior pointwise quantiles, and extended developments to simultaneous quantile credible intervals by rescaling of the bounds of the pointwise credible intervals by a common factor.

The parametric and quantile credible intervals, used to describe uncertainty of the functional posterior estimates, have some drawbacks. Parametric credible intervals are by-design symmetric around the pointwise mean and are dependent on distributional assumptions that may not hold when modeling assumptions are violated. Quantile credible intervals allow for asymmetry using a rank-based approach, however they rely on pointwise ranks while approximating the ordering of a posterior sample of functions. To address these drawbacks, we propose central posterior envelopes (CPEs), which are not credible intervals, but are descriptive visualization tools to summarize the variation in the posterior summaries of the functional model components, contributing to uncertainty quantification in BFPCA. The proposed CPEs do not have to be symmetric around the estimated mean and are based on functional depth in ordering of a posterior sample of curves, rather than pointwise quantiles. Additionally, CPEs are formed using envelopes delineated by subsets of the posterior functional sample, and hence are fully data-driven, summarizing the variation in the posterior sample without any parametric assumptions.

Functional depth has been proposed to generalize order statistics to functional data, providing a center-outward order to a sample of functions (López-Pintado and Romo, 2009; Sun et al., 2012) and have been extended in a variety of FDA applications including construction of the median or a trimmed mean function, functional boxplots (Sun and Genton, 2012), surface boxplots (Genton et al., 2014), outlier detection via the outliergram (Arribas-Gil and Romo, 2014), robust rank, permutation and location tests for distributional and dispersion differences in two-sample functional data groups (López-Pintado and Wrobel, 2017; López-Pintado and Qian, 2020). López-Pintado and Romo (2009) introduced the notion of modified band depth (MBD), extending the definition of band depth based on a graph-based approach, by measuring the proportion of time that a curve lies in the band delimited by a subsample of curves. Sun

et al. (2012) derived a computationally efficient algorithm for calculating MBD that can rank millions of curves in seconds. Genton et al. (2014) further extended MBD to higher dimensional functional data through modified volume depth (MVD). We utilize both MBD and MVD to propose functional depth based CPEs for the mean function and eigenfunctions in BFPCA. MBD-CPEs are formed by ranking the posterior estimates and forming an envelope of a subset of the posterior estimates with the largest depth values. MVD-CPEs for eigenfunctions are formed via ranking of the posterior covariance surfaces.

The paper is organized as follows. The BFPCA model considered is introduced in Section 2 along with an outline of the traditional posterior summaries for the BFPCA model components. The considered BFPCA is a simplification of previous formulations in literature, where a Bayesian estimation for model components is followed by derivation of the estimated mean and eigenfunctions through singular value decomposition of the estimated covariance surfaces. The proposed model uses a latent factor model to represent the functional observations where the mean function and latent factors are further expanded on a basis set. A normal-inverse gamma prior is placed on the coefficients of the mean function, and a modified multiplicative gamma process shrinkage (MMGPS) prior is placed on the factor loadings to induce sparsity in basis selection similar to BLFRM. A computationally efficient estimation procedure is proposed for the considered BFPCA via fully conjugate priors that leads to implementation through a Gibbs sampler. The proposed CPEs based on functional depth are outlined in Section 3, followed by simulation studies to showcase their finite sample performance in the presence of different types of additional variation in the functional sample (Section 4). Section 5 outlines application of CPEs to analysis of a sample of power spectral densities (PSD) from resting state electroencephalography (EEG). Novel insights are provided on diagnostic group differences in the evolution of PSD across age among children diagnosed with autism spectrum disorder and their typically developing peers. A brief discussion is included in Section 6.

2 Bayesian Functional Principal Component Analysis

2.1 Model Specification

Let $Y_i(t) = f_i(t) + \epsilon_i(t)$ denote the observed noisy response measurements for subject i, $i = 1, \ldots, n$, represented as a sum of a smooth underlying function $f_i(t)$, and measurement error $\epsilon_i(t)$. The measurement error $\epsilon_i(t)$ is assumed to be i.i.d. with mean zero and variance σ_ϵ^2. The smooth function $f_i(t)$ is assumed to be square integrable with mean $\mu(t)$ and covariance $C(s,t) = \text{Cov}\{f_i(s), f_i(t)\} = \sum_{k=1}^{\infty} \rho_k \psi_k(s)\psi_k(t)$, where $\rho_1 \geqslant \rho_2 \geqslant \ldots$ denote the ordered nonnegative eigenvalues, and $\psi_1(t)$, $\psi_2(t)$, $\ldots$ denote the corresponding eigenfunctions. While the eigenfunctions describe direction of leading modes of variation in the functional data, the eigenvalues quantify the amount of variation explained by the different modes of variation. The Karhunen-Loève (KL) expansion of $f_i(t)$ is then given by $f_i(t) = \mu(t) + \sum_{k=1}^{\infty} \xi_{ik}\psi_k(t)$, where $\xi_{ik} = \int_t \{f_i(t) - \mu(t)\}\psi_k(t)dt$ denotes the kth subject-specific FPCA score with mean zero and variance ρ_k. In practice, the expansion is truncated to include K eigencomponents, $f_i(t) \approx \mu(t) + \sum_{k=1}^{K} \xi_{ik}\psi_k(t)$, based on fraction of variance explained (FVE), where the covariance is approximated by $C(s,t) \approx \sum_{k=1}^{K} \rho_k \psi_k(s)\psi_k(t)$. The first few eigencomponents are typically enough to explain the majority of variability in the data, leading to effective dimension reduction.

The BFPCA model considered is based on a latent factor model constructed for $f_i(t) = \mu(t) + \sum_{\ell=1}^{L} \eta_{i\ell}\phi_\ell(t)$, where $\phi_\ell(t)$, $\ell = 1, \ldots, L$, denote the L latent components and $\eta_{i\ell} \sim$

$N(0,1)$, $\ell = 1, \ldots, L$, denote the corresponding uncorrelated subject-specific scores. Next, the mean function and latent components are expanded on a set of R B-spline basis functions $(b_1(t), \ldots, b_R(t))$, $\mu(t) = \sum_{r=1}^{R} \beta_r b_r(t)$ and $\phi_\ell(t) = \sum_{r=1}^{R} \lambda_{r\ell} b_r(t)$, where β_r and $\lambda_{r\ell}$ denote the mean coefficients and factor loadings, respectively. This leads to the following expansion of $f_i(t) = \sum_{r=1}^{R}[\beta_r + \sum_{\ell=1}^{L} \eta_{i\ell}\lambda_{r\ell}]b_r(t)$, which in vector form can be given as the hierarchical model (James et al., 2000)

$$\begin{aligned} \boldsymbol{Y}_i &= \boldsymbol{f}_i + \boldsymbol{\epsilon}_i = B(\boldsymbol{\beta} + \Lambda\boldsymbol{\eta}_i) + \boldsymbol{\epsilon}_i, \\ \boldsymbol{\eta}_i &\sim N_L(\mathbf{0}_L, I_L), \quad \boldsymbol{\epsilon}_i \sim N_T(\mathbf{0}_T, \sigma_\epsilon^2 I_T), \quad i = 1, \ldots, n, \end{aligned} \tag{1}$$

where $\boldsymbol{Y}_i = \{Y_i(t_1), \ldots, Y_i(t_T)\}^\top$ denotes the response observed at a total of T time points, $\boldsymbol{f}_i = \{f_i(t_1), \ldots, f_i(t_T)\}^\top$ denotes the $T \times 1$ vector of underlying smooth functions and $\boldsymbol{\epsilon}_i = \{\epsilon_i(t_1), \ldots, \epsilon_i(t_T)\}^\top$ denotes the $T \times 1$ vector of measurement error. Furthermore, in (1), $B = (\mathbf{b}_1, \ldots, \mathbf{b}_R)$ denotes the $T \times R$ matrix of B-spline basis functions with $\mathbf{b}_r = \{b_r(t_1), \ldots, b_r(t_T)\}^\top$, $\boldsymbol{\beta} = (\beta_1, \ldots, \beta_R)^\top$ denotes the $R \times 1$ vector of mean coefficients, $\Lambda = (\boldsymbol{\lambda}_1, \ldots, \boldsymbol{\lambda}_L)$ denotes the $R \times L$ factor loading matrix with $\boldsymbol{\lambda}_\ell = (\lambda_{i\ell}, \ldots, \lambda_{R\ell})^\top$ and $\boldsymbol{\eta}_i = (\eta_{i1}, \ldots, \eta_{iL})^\top$ denotes the $L \times 1$ vector of subject-specific scores. Finally, $\mathbf{0}_L$ and $\mathbf{0}_T$ are used to denote the $L \times 1$ and $T \times 1$ vectors of zeros, respectively, and I_L and I_T are used to denote the $L \times L$ and $T \times T$ identity matrices.

Fully conditional conjugate priors on the variance components are selected to achieve efficient posterior estimation in BFPCA. More specifically, using Gaussian priors for the mean coefficients $\boldsymbol{\beta}$ and factor loadings $\boldsymbol{\lambda}_\ell$, noninformative prior for the error variance σ_ϵ^2 (proportional to some constant), gamma prior for the variance of the mean coefficients σ_β^2 and a modified multiplicative gamma process shrinkage (MMGPS) prior (Bhattacharya and Dunson, 2011; Montagna et al., 2012) for the variance components of the factor loading matrix $\sigma_{\lambda_{r\ell}}^2$,

$$\begin{aligned} &\boldsymbol{\beta} \sim N_R\left(\mathbf{0}_R, \frac{1}{\sigma_\beta^2}\Omega^{-1}\right), \quad \sigma_\beta^2 \sim \text{Gamma}\left(\frac{a_\beta}{2}, \frac{a_\beta}{2}\right), \quad \frac{1}{\sigma_\epsilon^2} \propto 1 \\ &\boldsymbol{\lambda}_\ell \sim N_R\left(\mathbf{0}_R, \Sigma_{\lambda_\ell}\right), \quad \Sigma_{\lambda_\ell} = \text{diag}(\sigma_{\lambda_{1\ell}}^2, \ldots, \sigma_{\lambda_{R\ell}}^2), \quad \sigma_{\lambda_{r\ell}}^2 = \varphi_{r\ell}^{-1}\tau_\ell^{-1}, \quad \varphi_{r\ell} \sim \text{Gamma}\left(\frac{\nu}{2}, \frac{\nu}{2}\right), \\ &\tau_\ell = \prod_{h=1}^{\ell} \delta_h, \quad \delta_1 \sim \text{Gamma}(a_1, 1), \quad \delta_h \sim \text{Gamma}(a_2, 1)I(\delta_h > 1), \quad h \geqslant 2, \end{aligned} \tag{2}$$

we target the posterior distributions in model (1) using a Gibbs sampler (posterior distributions and details on choice of hyperparameters, a_β, ν, a_1, a_2, are deferred to Supplementary Materials Appendix A). In (2), $\mathbf{0}_R$ denotes an $R \times 1$ vector of zeros, Ω is a positive-definite $R \times R$ penalty matrix, Σ_{λ_ℓ} is a $R \times R$ diagonal matrix comprised of the variance components, $\sigma_{\lambda_{1\ell}}^2, \ldots, \sigma_{\lambda_{R\ell}}^2$, for the ℓth factor loading $\boldsymbol{\lambda}_\ell$, and $I(\cdot)$ denotes the indicator function. The variance components of the factor loading matrix, denoted by $\sigma_{\lambda_{r\ell}}^2$, are given a MMGPS prior adapted from Bhattacharya and Dunson (2011), where $\varphi_{r\ell}$ and τ_ℓ denote the element-wise and column-wise precisions, respectively. The column-wise precision τ_ℓ is the cumulative product of gamma distributed δ_h for $h = 1, \ldots, \ell$. The truncation of δ_h to be larger than one when $h \geqslant 2$ guarantees that τ_ℓ increases with ℓ, forcing columns of Λ, $\boldsymbol{\lambda}_\ell$, to get stochastically smaller as ℓ increases. Note that this mimics the estimation of eigenfunctions in FPCA with ordered (decreasing) eigenvalues and results in effective basis selection (Montagna et al., 2012).

Based on empirical studies, Shamshoian et al. (2022) report that the estimation of the mean function and the covariance surface is robust to different choices of R, the total number of basis

functions used in the expansion. Following guidance from Shamshoian et al. (2022), R is selected to be a fraction of the total number of time points T, $R = \lfloor T/2 \rfloor$, for adequate smoothing of $f_i(t)$, provided L is large. In particular, the MMGPS prior is robust when the choice of L is large, but if L is chosen to be too small, then the MMGPS prior may not be robust and lead to potentially unreliable posterior estimates (Bhattacharya and Dunson, 2011; Montagna et al., 2012). Note that in the BFPCA formulation in (1), the total number of latent components L are typically larger than K, the number of eigencomponents retained in the FPCA expansion. Thus, following results in Shamshoian et al. (2022) and considering the properties of the MMGPS prior, L is selected to be a fraction of R, $L = max(6, \lfloor R/4 \rfloor)$, where the lower bound of $L = 6$ should be a sufficiently large enough number of latent components when R is relatively small.

2.2 Traditional Posterior Summaries for BFPCA Components

Posterior estimates of the mean coefficient vector $\boldsymbol{\beta}^{(m)} = (\beta_1^{(m)}, \ldots, \beta_R^{(m)})^\top$ and factor loading matrix $\Lambda^{(m)} = (\boldsymbol{\lambda}_1^{(m)}, \ldots, \boldsymbol{\lambda}_L^{(m)})$, with $\boldsymbol{\lambda}_\ell^{(m)} = (\lambda_{1\ell}^{(m)}, \ldots, \lambda_{R\ell}^{(m)})^\top$, where the superscript $m, m = 1, \ldots, M$, is used to index the posterior estimates obtained from the MCMC sampler after burn-in and thinning, leads to the posterior estimates of the mean function, $\mu^{(m)}(t) = \sum_{r=1}^{R} \beta_r^{(m)} b_r(t)$, and the covariance $C^{(m)}(s,t) = \sum_{r=1}^{R}\sum_{r'=1}^{R}\sum_{\ell=1}^{L} \lambda_{r\ell}^{(m)}\lambda_{r'\ell}^{(m)} b_r(s) b_{r'}(t)$. In an attempt to recover the additional interpretations offered by the lower dimensional representation of FPCA (where eigenfunctions describe the leading modes of variation in the functional data), we consider the singular value decomposition of $C^{(m)}(s,t) \approx \sum_{k=1}^{K} \rho_k^{(m)} \psi_k^{(m)}(s)\psi_k^{(m)}(t)$, targeting the posterior estimates of the eigenfunctions, $\psi_k^{(m)}(t)$, and eigenvalues, $\rho_k^{(m)}$ (Suarez and Ghosal, 2017). The total number of eigencomponents retained, K, is chosen by the mean or the median FVE calculated across the posterior samples. Since the sign of the eigenfunctions are not identifiable, we implement an additional alignment step in obtaining the posterior estimates of the eigenfunctions (see Supplementary Materials Appendix B for further details).

The mean estimate is obtained by averaging the posterior estimates, $\widehat{\mu}(t) = (1/M)\sum_{m=1}^{M} \mu^{(m)}(t)$. The eigenfunctions and eigenvalues can be targeted in two ways. The first approach is to average the posterior estimates, $\widehat{\psi}_k(t) = (1/M)\sum_{m=1}^{M} \psi_k^{(m)}(t)$, $\widehat{\rho}_k = (1/M)\sum_{m=1}^{M} \rho_k^{(m)}$, $k = 1, \ldots, K$, similar to the mean estimate. An alternative approach is to first target the mean of the posterior covariances, $\widetilde{C}(s,t) = (1/M)\sum_{m=1}^{M} C^{(m)}(s,t)$, followed by SVD of $\widetilde{C}(s,t) \approx \sum_{k=1}^{K} \widetilde{\rho}_k \widetilde{\psi}_k(s)\widetilde{\psi}_k(t)$, leading to the eigenfunction and eigenvalue estimates obtained via covariance estimation, denoted by $\widetilde{\psi}_k(t)$ and $\widetilde{\rho}_k$, respectively. While we evaluate the finite sample performance of both point estimates for the eigenfunctions and eigenvalues via simulations, we center the traditional credible intervals for these quantities around the posterior average estimates.

A main advantage of BFPCA is the readily available inference provided for the FPCA components based on the posterior sample. While credible intervals can be constructed for the scalar components (including eigenvalues or FVE) using the standard deviation or percentiles obtained from the posterior sample, we center our discussion mainly on inference for the functional components, which is the focus of the proposed functional depth based approach. For the functional components of FPCA, i.e. the mean and eigenfunctions, traditional posterior summaries include pointwise and simultaneous, parametric and quantile credible intervals. In the formulations below, parametric and quantile credible intervals will be denoted by capital 'P' and 'Q', respectively, for ease of notation, while pointwise and simultaneous credible intervals will be distinguished by the superscripts 'p' and 's'. While the parametric intervals are based on variance of the estimates in the posterior sample, the quantile intervals leverage pointwise quantiles obtained from the posterior sample. Let $g(t)$ denote either the mean or eigenfunction of

interest, observed at time points t_j, $j = 1, \ldots, T$, and let $\widehat{g}(t_j)$ and $\widehat{Var}\{g(t_j)\}$ denote the sample mean and variance of $g(t_j)$ calculated from the M MCMC samples $g^{(m)}(t)$. The $(1-\alpha)100\%$ pointwise parametric credible interval for $g(t)$ is given by $[\widehat{g}(t_j) \pm z_\alpha \sqrt{\widehat{Var}\{g(t_j)\}};\ j = 1, \ldots, T]$ (denoted as $P^p_{1-\alpha}\{g(t)\}$), where $z_\alpha = \Phi^{-1}(1-\alpha/2)$ with Φ denoting the cumulative distribution function of the standard normal distribution. For defining the simultaneous parametric credible intervals, let c_α denote the $(1-\alpha)$ sample quantile of $\max_{j=1,\ldots,T} \mid \{g^{(m)}(t_j) - \widehat{g}(t_j)\}/\sqrt{\widehat{Var}\{g(t_j)\}} \mid$ over the M posterior samples. Then the $(1-\alpha)100\%$ simultaneous parametric credible interval for $g(t)$ is given by $[\widehat{g}(t_j) \pm c_\alpha \sqrt{\widehat{Var}\{g(t_j)\}};\ j = 1, \ldots, T]$ (denoted as $P^s_{1-\alpha}\{g(t)\}$) (Crainiceanu et al., 2007).

For the pointwise and simultaneous quantile credible intervals, let $g_{\alpha/2}(t_j)$ and $g_{1-\alpha/2}(t_j)$ denote the pointwise $\alpha/2$ and $(1-\alpha/2)$ sample quantiles of $g^{(m)}(t)$, $m = 1, \ldots, M$ at $t = t_j$, respectively. Then $(1-\alpha)100\%$ pointwise quantile credible interval for $g(t)$ is given by $[\{g_{\alpha/2}(t_j), g_{1-\alpha/2}(t_j)\};\ j = 1, \ldots, T]$ (denoted as $Q^p_{1-\alpha}\{g(t)\}$). The $(1-\alpha)100\%$ simultaneous quantile credible interval for $g(t)$ is given by $[\widehat{g}(t_j) + q\{g_{\alpha/2}(t_j) - \widehat{g}(t_j)\}, \widehat{g}(t_j) + q\{g_{1-\alpha/2}(t_j) - \widehat{g}(t_j)\};\ j = 1, \ldots, T]$ (denoted as $Q^s_{1-\alpha}\{g(t)\}$), where q is a common factor that rescales the upper and lower bounds until $(1-\alpha)100\%$ of the posterior estimates are contained inside the credible interval (Krivobokova et al., 2010). Note that the factor q is common across all time points t_j in the above formulation and that both pointwise and simultaneous quantile credible intervals rely on pointwise quantiles while trying to quantify uncertainty in estimation of a functional component. The proposed central posterior envelopes based on functional depth consider ranking of the entire functional estimates in the posterior sample, rather than relying on pointwise quantiles. The code for implementation of the quantile credible intervals can be found in the R package *acid*. The notations used for the traditional posterior summaries outlined above, as well as the functional depth based intervals proposed in the next section, are summarized for the readers reference in Supplementary Materials Table S1.

3 Proposed Functional Depth Based CPEs for BFPCA

The traditional posterior summaries outlined in Section 2.2 have potential pitfalls when describing posterior distributions of functional data. The parametric credible intervals rely on distributional assumptions, which may be violated under deviation from modeling assumptions. In addition, the parametric credible intervals are symmetric around the pointwise mean, which is restrictive when capturing potential asymmetry in posterior distributions in the presence of highly variable and/or skewed posterior samples. Although the quantile credible intervals are data-driven and more flexible with potential asymmetry, their construction relies on pointwise quantiles. In particular, instead of treating posterior samples as functional data, the quantile credible intervals are estimated by ranking of the posterior samples at each time point. Furthermore, scaling the pointwise quantiles by a common factor q across all time points in construction of the simultaneous quantile credible intervals may be too restrictive in modeling the spread in the functional posterior samples. In order to circumvent these issues, the use of functional depth is proposed to rank the functional posterior estimates to obtain fully data-driven CPEs that capture uncertainty in a flexible way.

Functional depth is a measure that provides a center-outward ordering of a sample of functional observations. In particular, functional depth ranks a sample of functions from the 'deepest' curve with the highest functional depth value, defined as the median curve, to the

most outlying curve with the lowest functional depth value. Although there are a number of functional depth measures that have been proposed in the literature (see Zuo and Serfling (2000) and Gijbels and Nagy (2017)), modified band depth based on a graph-based approach has been quite popular in applications López-Pintado and Romo (2009). Let $g^{(1)}(t)$, …, $g^{(M)}(t)$, $t \in \mathcal{I}$, denote a sample of M functional posterior estimates, either for the mean or eigenfunctions, defined on a compact interval $\mathcal{I}$, where $\mathcal{I} \in \mathbb{R}$. The band in $\mathbb{R}^2$ delineated by a subset of u, $2 \leqslant u \leqslant M$, posterior estimates, $g^{(m_1)}(t)$, …, $g^{(m_u)}(t)$, drawn from the full posterior sample $\{g^{(1)}(t), \ldots, g^{(M)}(t)\}$ is given by

$$\mathcal{B}\left\{g^{(m_1)}(t), \ldots, g^{(m_u)}(t)\right\} = \left[\{t, g(t)\} : t \in \mathcal{I}, \min_{v=m_1,\ldots,m_u} g^{(v)}(t) \leqslant g(t) \leqslant \max_{v=m_1,\ldots,m_u} g^{(v)}(t)\right].$$

Supplementary Materials Figures S1 (a) and (b) represent two bands $\mathcal{B}\left\{g^{(1)}(t), g^{(2)}(t)\right\}$ and $\mathcal{B}\left\{g^{(3)}(t), g^{(4)}(t)\right\}$, delimited by two curves, where in the first figure the entire graph of $g^{(m)}(t)$ and in the second a proportion of it is included in the band. Band depth of López-Pintado and Romo (2009) considers the proportion of bands $\mathcal{B}\left\{g^{(m_1)}(t), \ldots, g^{(m_u)}(t)\right\}$ determined by u different curves $g^{(m_1)}(t)$, …, $g^{(m_u)}(t)$ containing the graph of $g(t)$. Modified band depth (MBD) extends band depth, such that rather than the proportion of bands that contain the entire graph of $g(t)$, MBD considers the proportion of time that the graph of $g(t)$ lies inside the bands. More specifically, let

$$\mathcal{A}_u\left\{g^{(m)}(t); g^{(m_1)}(t), \ldots, g^{(m_u)}(t)\right\} = \left\{t \in \mathcal{I} : \min_{v=m_1,\ldots,m_u} g^{(v)}(t) \leqslant g^{(m)}(t) \leqslant \max_{v=m_1,\ldots,m_u} g^{(v)}(t)\right\},$$

denote the set in the interval $\mathcal{I}$ where the function $g^{(m)}(t)$ lies inside the band $\mathcal{B}\{g^{(m_1)}(t), \ldots, g^{(m_u)}(t)\}$. Further, let

$$\mathcal{A}_u^*\left\{g^{(m)}(t); g^{(m_1)}(t), \ldots, g^{(m_u)}(t)\right\} = \theta\left[\mathcal{A}_u\left\{g^{(m)}(t); g^{(m_1)}(t), \ldots, g^{(m_u)}(t)\right\}\right]/\theta\left(\mathcal{I}\right),$$

denote the proportion of time that the curve $g^{(m)}(t)$ lies inside the band $\mathcal{B}\{g^{(m_1)}(t), \ldots, g^{(m_u)}(t)\}$, where $\theta(\cdot)$ denotes the Lebesgue measure on $\mathcal{I}$. If $2 \leqslant U \leqslant M$ denotes a fixed total number of curves used to delineate a band, then the modified band depth (MBD) for the curve $g^{(m)}(t)$ in $g^{(1)}(t)$, …, $g^{(M)}(t)$ given U is

$$\mathrm{MBD}_{M,U}\left\{g^{(m)}(t)\right\} = \sum_{u=2}^{U}\left[\binom{M}{2}^{-1} \sum_{1 \leqslant m_1 < m_2 < \cdots < m_u \leqslant M} \mathcal{A}_u^*\left\{g^{(m)}(t); g^{(m_1)}(t), \ldots, g^{(m_u)}(t)\right\}\right].$$

MBD ranks each curve in the sample $g^{(1)}(t)$, …, $g^{(M)}(t)$ as the sum of $\mathcal{A}_u^*\{g^{(m)}(t); g^{(m_1)}(t), \ldots, g^{(m_u)}(t)\}$ over all possible combinations of bands delineated by $2 \leqslant U \leqslant M$ total curves that can be formed. Functions where a higher proportion of the curve lies in a higher number of bands get a higher MBD value, representing curves that are closer to the center of the sample. Those curves with lower MBD values have a lower proportion of the curve lying in a lower proportion of bands, representing outlying observations, resulting in an effective ranking of the sample. We follow common practice and set $U = 2$ in applications for computational efficiency (and drop U from the MBD notation), where bands delineated by all combinations of two curves are considered in the MBD definition (i.e. $\mathrm{MBD}_M\{g^{(m)}(t)\} \equiv \mathrm{MBD}_{M,2}\{g^{(m)}(t)\}$) (López-Pintado and Romo, 2009).

MBD of the posterior estimates are utilized to obtain point estimates (i.e. MBD median) and functional band depth central posterior envelopes (i.e. MBD-CPEs for the BFPCA functional

Algorithm 1: MBD Median and MBD-CPE for $g(t) \equiv \mu(t)$ or $g(t) \equiv \psi_k(t)$

Step 1: Calculate the MBD of the posterior samples: $\text{MBD}_M\{g^{(1)}(t)\}, \ldots, \text{MBD}_M\{g^{(M)}(t)\}$.

Step 2: Order the MBD values of the posterior sample from the smallest to the largest and denote the corresponding ordered samples as $g^{[1]}(t), \ldots, g^{[M]}(t)$.

Step 3: Calculate the $(1-\alpha)100\%$ MBD-CPE as

$$D_{1-\alpha}\{g(t)\} = B\left\{g^{[\lfloor \alpha M \rfloor + 1]}(t), \ldots, g^{[M]}(t)\right\},$$

and the MBD median as $\widehat{m}\{g(t)\} = g^{[M]}(t)$.

components ($\mu(t)$ and $\psi_k(t)$). While the MBD median equals the functional median of the posterior sample, the $(1-\alpha)100\%$ MBD-CPE is formed by the band delineated by the $1-\alpha$ deepest posterior estimates in the sample. The MBD median and $(1-\alpha)100\%$ MBD-CPE formed for the functional BFPCA component $g(t)$, denoted by $\widehat{m}\{g(t)\}$ and $D_{1-\alpha}\{g(t)\}$, respectively, are targeted via Algorithm 1. *Note that similar to functional depth based central envelopes proposed for functional data, CPEs are not credible intervals, but they rather are descriptive visualization tools that help summarize the variation in the posterior sample. When plotted for a grid of α values, CPEs display the central envelopes allowing for visualization of the most central regions of the functional posterior distributions.*

An alternative way for obtaining point estimates and CPEs for the eigenfunctions $\psi_k(t)$, $k = 1, \ldots, K$, is to rank the posterior covariance surfaces using modified volume depth (MVD). MBD has been extended to surface data as MVD to provide a way to rank two-dimensional functional data (Sun et al., 2012; Genton et al., 2014) (for extensions to higher-dimensional functional data, see López-Pintado and Wrobel (2017)). Let $C^{(1)}(s,t), \ldots, C^{(M)}(s,t)$, $(s,t) \in \mathcal{S}$, denote a sample of M posterior covariance estimates, defined on $\mathcal{S} \in \mathbb{R}^2$. Further, let

$$\begin{aligned}&\mathcal{A}_u\left\{C^{(m)}(s,t); C^{(m_1)}(s,t), \ldots, C^{(m_u)}(s,t)\right\}\\ &\quad= \left\{(s,t) \in \mathcal{S} : \min_{v=m_1,\ldots,m_u} C^{(v)}(s,t) \leqslant C^{(m)}(s,t) \leqslant \max_{v=m_1,\ldots,m_u} C^{(v)}(s,t)\right\},\end{aligned}$$

denote the region in $\mathcal{S}$ where the covariance $C^{(m)}(s,t)$ lies inside the simplex delineated by the covariances $C^{(m_1)}(s,t), \ldots, C^{(m_u)}(s,t)$. In addition,

$$\begin{aligned}&\mathcal{A}_u^*\left\{C^{(m)}(s,t); C^{(m_1)}(s,t), \ldots, C^{(m_u)}(s,t)\right\}\\ &\quad= \vartheta\left[\mathcal{A}_u\left\{C^{(m)}(s,t); C^{(m_1)}(s,t), \ldots, C^{(m_u)}(s,t)\right\}\right]/\vartheta\left(\mathcal{S}\right),\end{aligned}$$

is used to denote the proportion of time that the covariance $C^{(m)}(s,t)$ lies inside the simplex formed by the covariances $C^{(m_1)}(s,t), \ldots, C^{(m_u)}(s,t)$, where $\vartheta(\cdot)$ denotes the Lebesgue measure extended to $\mathbb{R}^2$. Considering $U = 2$ total covariances to delineate a simplex (similar to the definition of MBD), MVD for the covariance $C^{(m)}(s,t)$ in $C^{(1)}(s,t), \ldots, C^{(M)}(s,t)$ is given as

$$\text{MVD}_M\left\{C^{(m)}(s,t)\right\} = \binom{M}{2}^{-1} \sum_{1 \leqslant m_1 < m_2 \leqslant M} \mathcal{A}_2^*\left\{C^{(m)}(s,t); C^{(m_1)}(s,t), C^{(m_2)}(s,t)\right\}.$$

MVD of the posterior covariance estimates are utilized to obtain point estimates (i.e. MVD median) and functional volume depth CPEs (i.e. MVD-CPEs) for $\psi_k(t)$, $k = 1, \ldots, K$. The MVD median and $(1-\alpha)100\%$ MVD-CPE formed for $\psi_k(t)$, denoted by $\widetilde{m}\{\psi_k(t)\}$ and $D^{\star}_{1-\alpha}\{\psi_k(t)\}$,

Algorithm 2: MVD Median and MVD-CPE for $\psi_k(t)$

Step 1: Calculate the MVD of the posterior covariances:

$$\text{MVD}_M\{C^{(1)}(s,t)\}, \ldots, \text{MVD}_M\{C^{(M)}(s,t)\}.$$

Step 2: Order the MVD values of the posterior sample from smallest to largest and denote the corresponding covariances as $C^{[1]}(s,t)$, …, $C^{[M]}(s,t)$.

Step 3: The SVD of the ordered covariances lead to their corresponding ordered eigenfunctions $\psi_k^{[1]}(t)$, …, $\psi_k^{[M]}(t)$.

Step 4: Calculate the $(1-\alpha)100\%$ MVD-CPE as

$$D^{\star}_{1-\alpha}\{\psi_k(t)\} = B\left\{\psi_k^{[\lfloor \alpha M \rfloor + 1]}(t), \ldots, \psi_k^{[M]}(t)\right\},$$

and the MVD median as $\widetilde{m}\{\psi_k(t)\} = \psi_k^{[M]}(t)$.

respectively, are targeted via Algorithm 2. The algorithm starts with ranking the posterior covariances using MVD and obtaining their corresponding eigenfunctions. The MVD median for $\psi_k(t)$ equals the functional median of the posterior eigenfunctions, while the $(1-\alpha)100\%$ MBD-CPE for $\psi_k(t)$ is formed by the band delineated by the $1-\alpha$ deepest eigenfunction estimates in the sample, where the eigenfunction estimates are ordered according to MVD of their corresponding posterior covariances.

Functional depth based medians proposed above ($\widehat{m}\{\mu(t)\}$, $\widehat{m}\{\psi_k(t)\}$ and $\widetilde{m}\{\psi_k(t)\}$) estimate the central tendency in the posterior distributions of the mean and eigenfunctions and provide a realistic estimate equal to one of the observed functional posterior samples rather than relying on pointwise averages as is done in most of the traditional posterior summaries. In addition, the proposed functional depth based CPEs (denoted by $D_{1-\alpha}\{g(t)\}$ and $D^{\star}_{1-\alpha}\{\psi_k(t)\}$, corresponding to MBD and MVD based summaries, respectively), are formed from a band delineated from the $1-\alpha$ deepest subset of the functional posterior estimates. Hence, the proposed methods use functional depth measures to construct fully data-driven summaries that capture the uncertainty in the posterior estimates in a flexible way. Notations used for point estimates and credible intervals both in the traditional summaries and in the proposals are summarized in Supplementary Materials Table S1.

4 Simulation Studies

We consider five simulation scenarios to display the use of CPEs in describing the variation in the posterior samples. We also study the finite sample properties of the traditional summaries from Section 2.2 under different simulation scenarios. More specifically five simulation scenarios are proposed: Case 1 – no additional variation in the i.i.d functional sample, Case 2 – additional constant variation, Case 3 – variation added through eigenvalues, Case 4 – variation added through time-shifted eigenfunctions, Case 5 – variation added through higher-frequency eigenfunctions. Case 2 generates observations with added variation by adding a constant deviation (with a random sign) to $\mu(t)$ for $t \geqslant T_i$, where $T_i \sim \text{Unif}[0,1]$. This adds constant variation to randomly selected portions of the unit time domain in $[0,1]$, where more of the variation is added to the latter part of the domain. Case 3 generates observations with additional variation using larger eigenvalues ρ_k, which result in increased variation throughout the unit interval. Fi-

nally, observations with additional variation are generated from time-shifted (Case 4) or higher frequency (Case 5) eigenfunctions in Cases 4 and 5, where additional variation is added along the direction of the time-shifted or higher frequency eigenfunctions used. Results are reported for simulation cases where observations with additional variation constitute $q = 10$ and 20% of the functional sample ($n = 50$), where details of data generation under the five simulation scenarios are deferred to the Supplementary Materials (Appendix C).

The BFPCA model is fitted using $R = 20$ B-spline basis functions with equidistant knots in $[0, 1]$ and $L = 6$ latent factors, for functional data observed on a uniform grid of 40 time points. Results are reported based on a total of 200 Monte Carlo runs with $25,000$ MCMC iterations ($5,000$ for burn-in and thinning at every 5th iteration), and $M = 4,000$ posterior estimates for each Monte Carlo run. The number of eigencomponents K selected for each simulation case was based on a fixed cutoff of 90% FVE explained. While the leading two eigencomponents explained more than 90% variation in the data in simulation cases 1, 3 and 4, the leading three eigencomponents were retained to explain 90% variation in cases 2 and 5. Finite sample performance of point estimates of the functional model components (i.e. mean and eigenfunctions) and scalar model components (i.e. eigenvalues) are assessed via the standardized integrated mean squared error (IMSE) and the standardized mean squared error (MSE), respectively. The mean IMSE and MSE values from 200 Monte Carlo runs for the five simulation scenarios are summarized in Supplementary Materials Table S2. The traditional and proposed point estimates for the mean function and the three leading eigenfunctions from the Monte Carlo run with the median IMSE are given in Supplementary Materials Figure S2, S3, S4 and S5, respectively. The discussion on the finite sample performance of the point estimates are deferred to Supplementary Materials Appendix C.

We assess how well traditional credible intervals and proposed CPEs reflect variation in the posterior sample under the five simulation scenarios. Supplementary Materials Figure S6, Figures 1, 2 and Figure S7 display CPEs from α cutoffs ranging from 0.05 to 0.95 for the mean function and the leading three eigenfunctions, respectively, from a single Monte Carlo run overlaying $M = 4,000$ posterior estimates (given in gray) for the five simulation scenarios (for $q = 20\%$). In addition, Supplementary Materials Figures S8, S9, S10 and S11 display the 95% parametric and quantile credible intervals and 95% CPEs for reference, for the mean function and the leading three eigenfunctions, respectively, from a single Monte Carlo run overlaying $M = 4,000$ posterior estimates for the five simulation scenarios (for $q = 20\%$). CPEs from increasing α cutoffs help visualize regions with the most central functional posterior observations in the sample. Note that while MBD-CPEs for the eigenfunctions are nested in each other for increasing α values, MVD-CPEs are not necessarily nested since they are based on the functional depth rankings of the posterior covariance surfaces, rather than posterior eigenfunctions. This is also the reason why MVD-CPEs are typically wider than MBD-CPEs, incorporating variation from the entire covariance process, rather than only eigenfunction-specific variation.

The added variation in the posterior estimates of especially the eigenfunctions really help portray the shortcomings of the symmetry restrictions and constant multipliers used in enlarging of the simultaneous parametric and quantile credible intervals, respectively. Figures S9 and S10 (d), (g), (j) and (m) show that the symmetry restriction (around the pointwise mean) of the parametric credible intervals force the credible intervals to be too wide in one bound and too narrow in the other, especially when the variation in the posterior sample is not symmetric. While the quantile credible intervals perform better relative to their parametric counter parts, they also include regions that do not represent posterior sample variation, perhaps due to the restrictive enlargement of the credible intervals by a constant multiplier that is kept the same

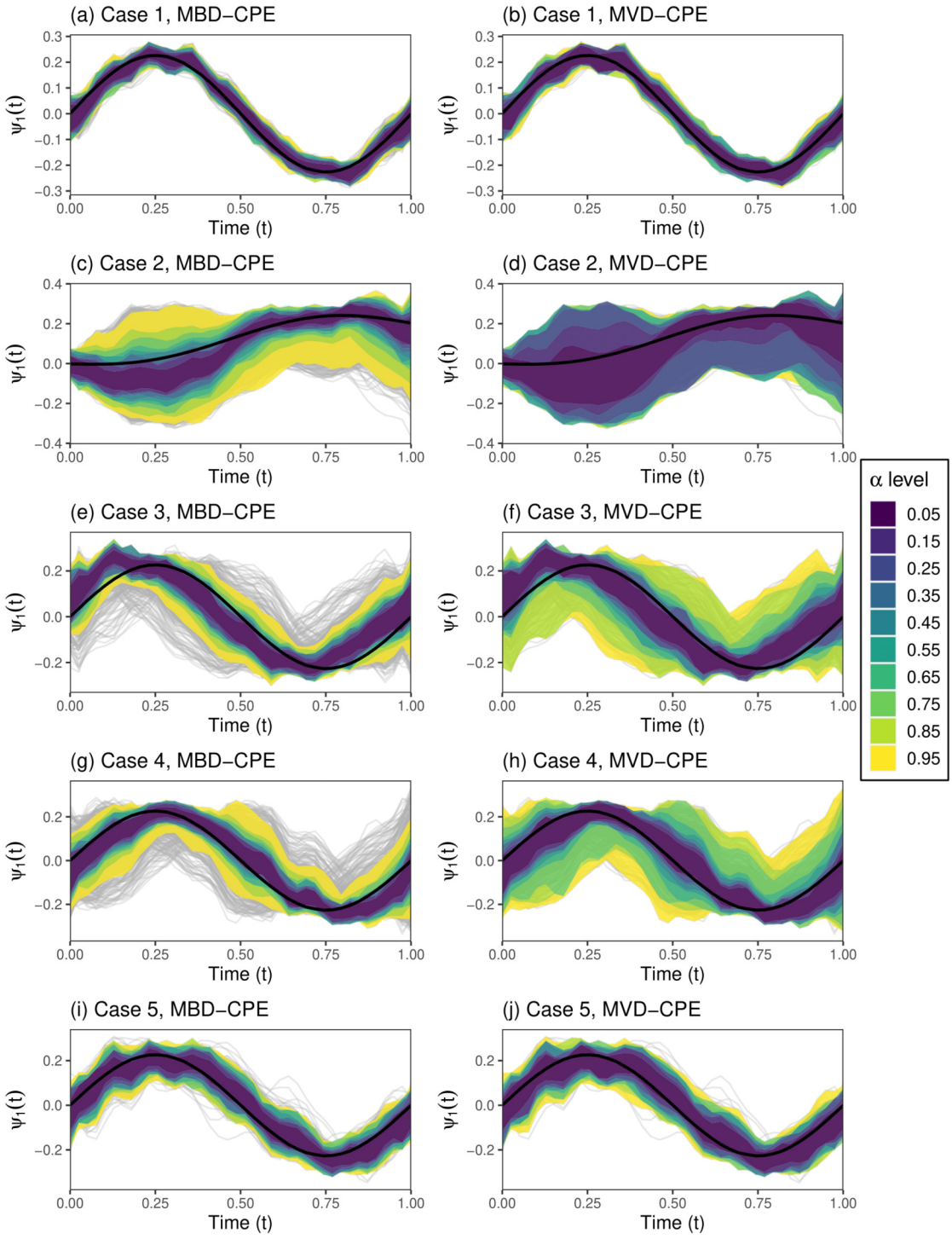

Figure 1: CPE contours of $\psi_1(t)$ for each simulation case with $q = 20\%$ of observations with added variation. The light grey solid lines, overlaying the true function in solid black, represent the sample of $M = 4000$ posterior estimates. The left and right hand columns display the MBD and MVD-CPEs, denoted by $D_{1-\alpha}\{\psi_1(t)\}$ and $D^{\star}_{1-\alpha}\{\psi_1(t)\}$, respectively, at a grid of α levels marked by varying contour colors.

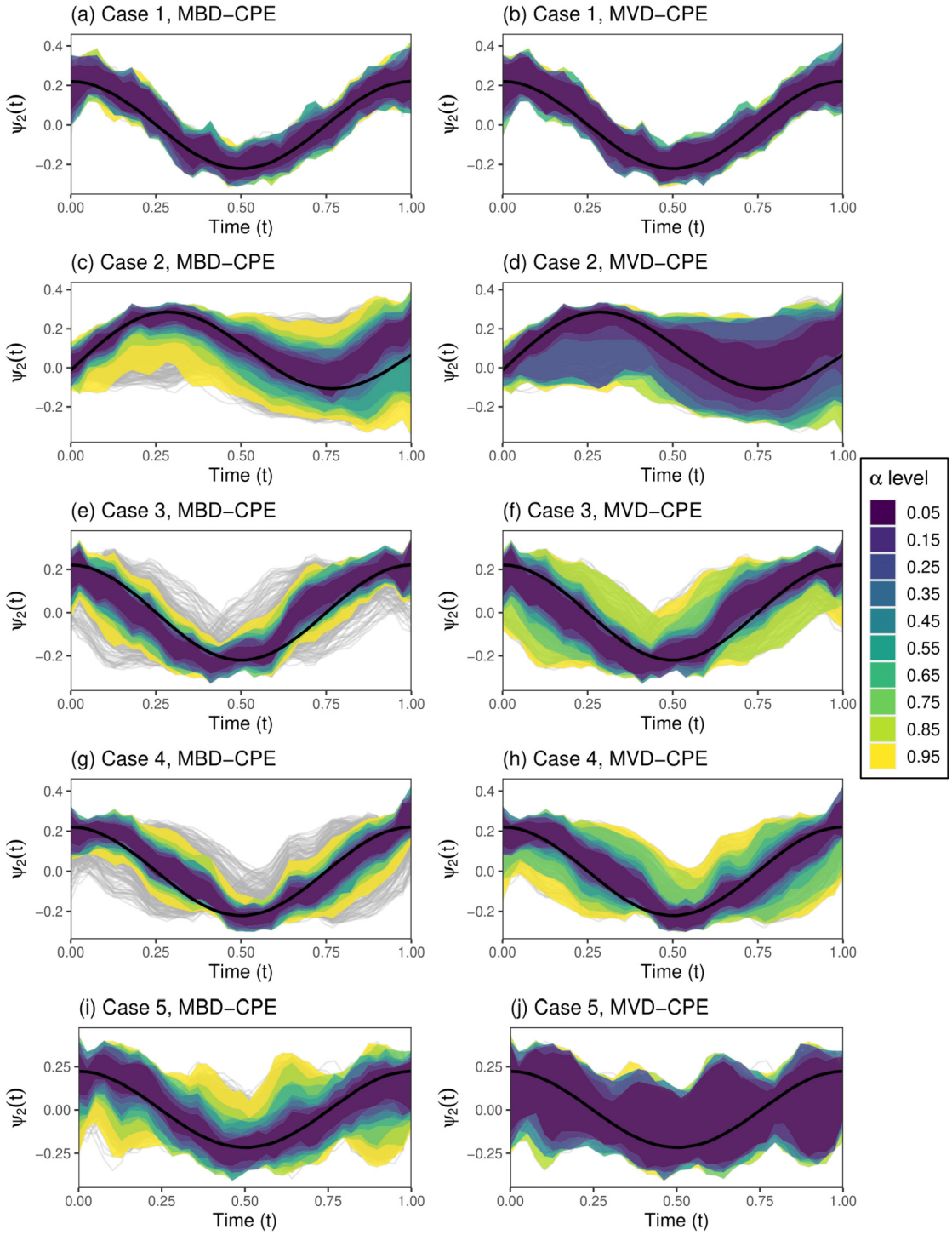

Figure 2: CPE contours of $\psi_2(t)$ for each simulation case with $q = 20\%$ of observations with added variation. The light grey solid lines, overlaying the true function in solid black, represent the sample of $M = 4000$ posterior estimates. The left and right hand columns display the MBD and MVD-CPEs, denoted by $D_{1-\alpha}\{\psi_1(t)\}$ and $D^{\star}_{1-\alpha}\{\psi_1(t)\}$, respectively, at a grid of α levels marked by varying contour colors.

over the entire time domain. The latter point is best observed in Table 1, reporting two metrics: negative area ratio (NAR) and area ratio (AR). NAR and AR capture the ratio of the area of the credible interval or CPE that lies outside and inside of posterior sample (proportional to the area of the posterior sample), respectively. Hence, while higher AR values (AR $\in [0, 1]$) correspond to a more realistic portrayal of the variation in the posterior sample estimates in the presence of additional variation, NAR values greater than zero can signal problems with the credible intervals (i.e. via inclusion of regions that do not represent the posterior sample), possibly due to symmetry constraints. Similar to previous sections, let $g^{(1)}(t), \ldots, g^{(M)}(t)$ denote the M MCMC samples, where $g(t) \equiv \mu(t)$ or $\psi_k(t)$. In addition, denote the pointwise lower and upper bounds of the posterior sample by $g_{\min}(t_j) = \min_{m=1,\ldots,M}\{g^{(m)}(t_j)\}$ and $g_{\max}(t_j) = \max_{m=1,\ldots,M}\{g^{(m)}(t_j)\}$, respectively, at a total of T grid points t_j, $j = 1, \ldots, T$. Finally denote the pointwise lower and upper bounds of the discretized $(1-\alpha)100\%$ credible interval $H_{1-\alpha}\{g(t)\}$ by $H_{1-\alpha}\{g(t_j)\} = [L(t_j), U(t_j)]$ for t_j, $j = 1, \ldots, T$. Then NAR and AR are given as follows

$$\begin{aligned}\mathrm{NAR}[H_{1-\alpha}\{g(t)\}] &= \frac{\sum_{j=1}^{T}[\{U(t_j) - g_{\max}(t_j)\}I\{U(t_j) > g_{\max}(t_j)\}]}{\sum_{j=1}^{T}\{g_{\max}(t_j) - g_{\min}(t_j)\}} \\ &\quad + \frac{\sum_{j=1}^{T}[\{g_{\min}(t_j) - L(t_j)\}I\{g_{\min}(t_j) > L(t_j)\}]}{\sum_{j=1}^{T}\{g_{\max}(t_j) - g_{\min}(t_j)\}}\end{aligned}$$

$$\mathrm{AR}[H_{1-\alpha}\{g(t)\}] = \frac{\sum_{j=1}^{T}[\min\{U(t_j), g_{\max}(t_j)\} - \max\{L(t_j), g_{\min}(t_j)\}]}{\sum_{j=1}^{T}\{g_{\max}(t_j) - g_{\min}(t_j)\}}.$$

For the proposed CPEs and pointwise quantile credible intervals, NAR always equals zero, since these summaries are based on pointwise or functional ordering of the data and therefore have to lie within the posterior sample. However the simultaneous quantile credible intervals may have NAR values larger than zero, since the bounds of the pointwise quantile intervals are rescaled by a common factor that is constant across t_j. The mean NAR and AR values based on the 200 Monte Carlo runs across the five simulation scenarios are summarized in Table 1. In summary, simultaneous credible intervals lead to higher AR values than their pointwise counterparts (parametric and quantile), as expected, and have nonzero NAR values except for pointwise quantile credible intervals. This also confirms that they can cover regions not representing posterior sample variation as is observed from the figures. The CPEs have AR values equal to or larger than all traditional credible intervals and have NAR equal to zero by definition. Hence, CPEs provide a more flexible representation of the shape and spread of the posterior sample in the presence of added variability in estimation and can contribute to the visualization of the functional posterior sample in applications.

5 Data Application

We use CPEs in the analysis of EEG power spectral densities obtained on a sample of 58 children with autism spectrum disorder (ASD) and 39 of their typically developed (TD) peers at resting state (Dickinson et al., 2018). The goal of the study was to characterize the shift in the peak alpha frequency (PAF), a neurological biomarker defined as the location of a single prominent peak in the alpha frequency band (6–14Hz) of the spectral density, across development. It was of particular interest to compare ASD and TD groups in their evolution of the alpha peak across chronological age. PAF has been shown to shift from lower to higher frequencies as children

Table 1: The mean AR and NAR values for traditional and functional-depth based 95% credible intervals and CPEs over 200 Monte Carlo runs for all simulation cases with $q = \{10, 20\}\%$ of observations with added variation. $P^{p}_{1-\alpha}\{g(t)\}$, $P^{s}_{1-\alpha}\{g(t)\}$, $Q^{p}_{1-\alpha}\{g(t)\}$, $Q^{s}_{1-\alpha}\{g(t)\}$, $D_{1-\alpha}\{g(t)\}$ and $D^{\star}_{1-\alpha}\{g(t)\}$ denote the pointwise parametric and simultaneous credible intervals, quantile pointwise and simultaneous credible intervals, and MBD and MVD-CPEs, respectively.

			AR for $g(t)$						NAR for $g(t)$		
$g(t)$	q	Case	$P^{p}_{0.95}\{\cdot\}$	$P^{s}_{0.95}\{\cdot\}$	$Q^{p}_{0.95}\{\cdot\}$	$Q^{s}_{0.95}\{\cdot\}$	$D_{0.95}\{\cdot\}$	$D^{\star}_{0.95}\{\cdot\}$	$P^{p}_{0.95}\{\cdot\}$	$P^{s}_{0.95}\{\cdot\}$	$Q^{s}_{0.95}\{\cdot\}$
$\mu(t)$	-	Case 1	0.523	0.797	0.524	0.798	0.872	-	0.000	0.000	0.000
	10%	Case 2	0.524	0.789	0.525	0.790	0.908	-	0.000	0.000	0.000
		Case 3	0.523	0.792	0.524	0.793	0.866	-	0.000	0.000	0.000
		Case 4	0.522	0.793	0.523	0.795	0.868	-	0.000	0.000	0.000
		Case 5	0.523	0.802	0.523	0.803	0.891	-	0.000	0.000	0.000
	20%	Case 2	0.526	0.783	0.527	0.785	0.909	-	0.000	0.000	0.000
		Case 3	0.521	0.787	0.522	0.788	0.857	-	0.000	0.000	0.000
		Case 4	0.523	0.793	0.523	0.794	0.871	-	0.000	0.000	0.000
		Case 5	0.523	0.807	0.524	0.808	0.906	-	0.000	0.000	0.000
$\psi_1(t)$	-	Case 1	0.424	0.649	0.425	0.653	0.666	0.833	0.000	0.012	0.000
	10%	Case 2	0.472	0.692	0.480	0.702	0.740	0.922	0.007	0.067	0.007
		Case 3	0.428	0.648	0.429	0.652	0.659	0.842	0.001	0.016	0.000
		Case 4	0.435	0.651	0.437	0.658	0.662	0.863	0.002	0.029	0.001
		Case 5	0.422	0.662	0.423	0.663	0.703	0.857	0.000	0.005	0.000
	20%	Case 2	0.421	0.633	0.425	0.639	0.655	0.884	0.002	0.028	0.003
		Case 3	0.430	0.635	0.433	0.642	0.639	0.844	0.003	0.033	0.001
		Case 4	0.457	0.661	0.463	0.672	0.668	0.880	0.005	0.063	0.001
		Case 5	0.427	0.673	0.429	0.673	0.724	0.909	0.000	0.013	0.000
$\psi_2(t)$	-	Case 1	0.473	0.734	0.473	0.738	0.783	0.891	0.000	0.011	0.001
	10%	Case 2	0.561	0.793	0.568	0.799	0.856	0.980	0.010	0.111	0.010
		Case 3	0.471	0.724	0.472	0.730	0.764	0.893	0.001	0.014	0.001
		Case 4	0.479	0.726	0.481	0.734	0.757	0.907	0.001	0.026	0.002
		Case 5	0.472	0.733	0.472	0.735	0.788	0.947	0.001	0.028	0.002
	20%	Case 2	0.490	0.717	0.495	0.724	0.767	0.962	0.003	0.057	0.003
		Case 3	0.467	0.702	0.470	0.711	0.728	0.884	0.002	0.030	0.002
		Case 4	0.492	0.718	0.497	0.733	0.736	0.908	0.004	0.060	0.004
		Case 5	0.587	0.841	0.582	0.843	0.911	0.989	0.004	0.109	0.010
$\psi_3(t)$	10%	Case 2	0.518	0.772	0.521	0.781	0.828	0.984	0.003	0.058	0.008
		Case 5	0.503	0.799	0.505	0.800	0.872	0.995	0.001	0.035	0.004
	20%	Case 2	0.486	0.740	0.489	0.748	0.794	0.985	0.002	0.037	0.006
		Case 5	0.600	0.859	0.592	0.860	0.928	0.995	0.004	0.106	0.011

grow older in the TD group (Somsen et al., 1997; Stroganova et al., 1999; Dustman et al., 1999; Chiang et al., 2011; Cragg et al., 2011; Miskovic et al., 2015), however previous research has suggested that this chronological shift in the location of the PAF may be delayed or absent in children with ASD (Edgar et al., 2015). In our motivating study, electroencephalogram (EEG) data was sampled at 500Hz for 2 minutes using a 128-channel HydroCel Geodesic Sensor Net during an "eyes-open" resting-state paradigm in which bubbles were presented on a screen in a sound-attenuated room. The participants in the two diagnostic groups were age-matched with ages ranging from 25 to 146 months old with a median age of 66 and 65.8 months in the TD and ASD groups, respectively. To more generally capture the shape of the PSD in the alpha frequency band and to avoid the challenges involved in identifying a unique PAF for each subject, we consider scalp-averaged relative PSD from the alpha frequency band as our sample of functional data observed over $T = 33$ equidistant frequencies within 6–14Hz. The BFPCA model was estimated using $R = 16$ B-spline basis functions and $L = 6$ latent components, leading to $M = 4000$ posterior samples for each model component. Further information on pre-processing of the EEG data and the experiment are deferred to Supplementary Materials Appendix D.

Figures 3 (a) and (b) display a sample of the data obtained on 10 subjects from the TD and ASD diagnostic groups, respectively. Note that the data is quite noisy, where PAF is distinctly visible in only a subset of the subjects, where there is considerable variation in PAF and the amplitude of the alpha peak. Our goal is to summarize the mean and variation trends in the data using the BFPCA model and to characterize the variability in the posterior estimates of the model components using CPEs in both diagnostic groups. Given in Figure 3 (c) are the MBD-CPEs of the mean function at a grid of specified α-level contours in which both diagnostic groups were included in estimation. Additionally, in Figure 3 are the MBD median and 95% MBD-CPEs for the mean function estimated in age-based subgroups within the TD and ASD samples (Figures 3 (d) and (e), respectively). The age-based subgroups were obtained within each diagnostic group by using the group-specific median age. While the PAF of the estimated overall mean is around 9.5Hz, the trend in PAF across age-based subgroups is quite different within the TD and the ASD samples. While a clear developmental shift is observed in the TD sample (with PAF at 8.75 and 10.25Hz for young and old TD groups, respectively), the PAF in the ASD sample is quite similar across the two age-groups (observed around 9.5Hz). These results are consistent with previous literature and findings from our own work (Scheffler et al., 2019, 2022).

Next, we perform BFPCA on the entire sample and based on interpretations of the leading eigenfunctions using the proposed CPEs, we assess effects of age and diagnostic group on the leading eigenscores through regression analysis. The CPEs from α cutoffs ranging from 0.05 to 0.95 for the leading two eigenfunctions based on BFPCA on all subjects, overlaying $M = 4,000$ posterior estimates in gray, are given in Figure 4. The two leading eigencomponents explain more than 70% of the total variation with median and (2.5th, 97.5th) percentiles of FVE at 72.0% (66.9%, 76.5%). The CPEs of the third and fourth leading eigenfunctions, explaining 15.8% (12.6%, 19.6%) and 12.2% (9.7%, 15.0%) FVE, respectively, are deferred to Supplementary Materials Figure S12. While the leading eigenfunction mostly signals variation in the magnitude of the alpha peak around 10Hz (Figures 4 (a) and (b)), the second leading eigenfunction captures variation in PAF (location of the prominent alpha peak) and varies between 9Hz-10.75Hz (Figures 4 (c) and (d)). Note that the MVD-CPE envelopes are wider at lower alpha levels up to 0.55 and 0.45 for the first and second leading eigenfunctions, respectively, similar to the observations from our simulation study. For the reader's reference CPEs for the third and fourth leading eigenfunctions, capturing remaining variation in the concavity of the PSD in the alpha frequency

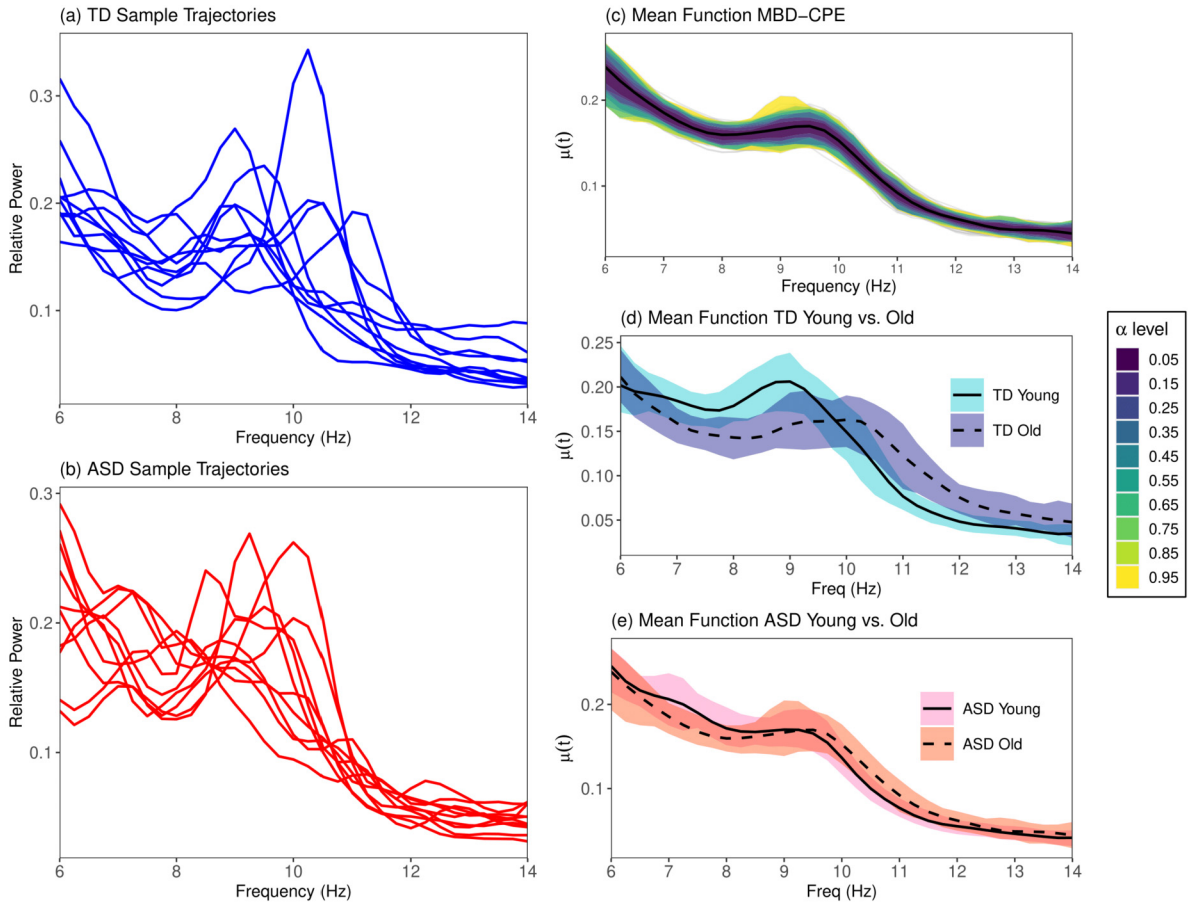

Figure 3: The left-hand columns display a sample of relative PSD obtained on 10 subjects from the TD (a) and ASD (b) diagnostic groups. The right-hand columns display the MBD-CPEs at a grid of α levels marked by varying contour colors for both TD and ASD groups (c) and estimated MBD medians (solid or dashed black lines) and 95% MBD-CPEs (colored area) for the mean function in the TD young and old groups (d) and ASD young and old groups (e).

band and 95% parametric and quantile credible intervals along with 95% CPEs are deferred to Supplementary Materials Figure S13. Consistent with results from the simulation section, simultaneous parametric credible intervals include regions that do not represent variation in the posterior sample (Figures S13 (g) and (j)).

Finally, in order to perform diagnostic group comparisons in the amount of variation in alpha peak amplitude and PAF, we regress the leading two eigenscores on diagnostic group (ASD), age (in months, mean-centered) and their interaction (see Supplementary Materials Table S3 for estimated regression components). Since a positive score on the leading eigenfunction indicates a larger amplitude of the prominent alpha peak, the positive regression coefficient of age (p-value: 0.0124) implies that older kids have larger alpha peak amplitudes across both diagnostic groups. The negative coefficient of ASD (p-value: 0.0354) indicates that the ASD group has a smaller amplitude of the alpha peak at the mean age of 70 months compared to the TD group. Since a negative score on the second leading eigenfunction indicates a later PAF, the negative regression coefficient of age (p-value: 0.0016) implies that the TD group displays the PAF shift from lower

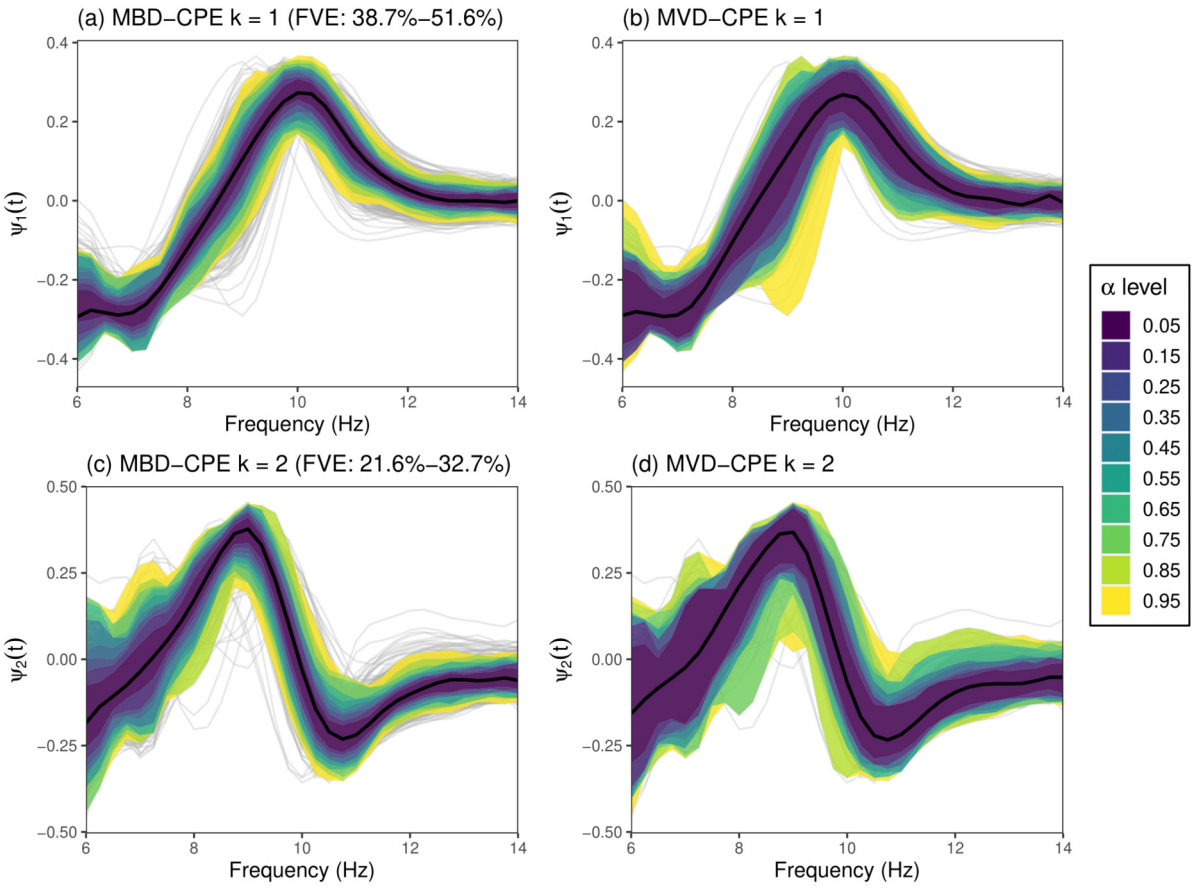

Figure 4: CPE contours of the two leading eigenfunctions for in our data application (with % FVE reported in (a) and (c)), overlaying the posterior estimates given in gray. The left and right hand columns display the MBD and MVD-CPEs, denoted by $D_{1-\alpha}\{\psi_1(t)\}$ and $D^{\star}_{1-\alpha}\{\psi_1(t)\}$, respectively, at a grid of α levels marked by varying contour colors. The estimated MBD and MVD median are given in solid black in the right and left columns, respectively.

to higher frequencies as the children age. This shift is not observed in the ASD group since the significant group by age interaction cancels this age effect in the ASD group.

6 Discussion

We propose a descriptive tool to visualize the variation in the posterior sample of the functional model components of BFPCA. The BFPCA modeling considered relies on a latent factor model and MMGPS priors on the variance components, leading to an easy to implement estimation framework and a direct way for inference on the model components. We recover the highly interpretable mean and eigenfunctions following Bayesian estimation and propose functional depth based summaries for these quantities. The novel summaries proposed are shown to lead to a data-driven approach in portraying the variability of the functional model components. Traditional summaries rely on distributional assumptions or suboptimal symmetry constraints, and fail to treat the posterior sample as functional data. In contrast, the proposed summaries

are based on ranking of the posterior sample for the functional components using functional depth. Two functional depth based summaries are considered, one based on direct ranking of the entire posterior functional sample and another through ranking of the associated covariance surfaces. Both approaches have been shown to lead to flexible modeling of the variation in the posterior sample, where the second leads to wider CPEs as expected, incorporating variation from the entire covariance process, rather than a single eigenfunction. Note that the proposed visualization tools are general and not model specific and hence can easily be applied to different formulations of BFPCA.

Extensions of the proposed methodology to higher dimensional functional data would be of interest, especially in EEG applications. EEG data is collected across the scalp, creating spatially indexed functional data. In addition, data are collected across multiple trials time locked to presentation of a sequence of stimuli in stimulus-based experiments and across time in resting state paradigms. When changes across experimental time are of interest, these repetitions can be viewed as an additional dimension of the observed data (i.e. as longitudinally observed functional data) and be part of analysis rather than collapsed via averaging. FPCA modeling has been considered for high-dimensional functional data, especially in EEG data applications involving a spatial or a longitudinal dimension (Shamshoian et al., 2022; Li et al., 2020; Campos et al., 2022; Scheffler et al., 2019, 2020; Hasenstab et al., 2017). Developments rely on simplifying assumptions on the higher dimensional covariance via strong or weak separability. The proposed functional depth based tools for visualization of the posterior sample can be extended to other Bayesian models of higher-dimensional functional data.

Supplementary Material

Supplementary material online includes: derived posterior distributions for model estimation; algorithm for alignment of posterior eigenfunction estimates; details on data generation for simulation studies and additional simulation results; pre-processing of the EEG data featured in Section 5; and plots illustrating band depth, and estimates from simulation studies and data analysis. The R code for the proposed methodology is made publicly available on the Github page https://github.com/dsenturk/FDpostSumms_BFPCA, along with a tutorial for step-by-step implementation using simulated data.

Funding

This research was supported by National Institute of Mental Health [R01 MH122428 (DS, DT, CS, SJ)].

References

Arribas-Gil A, Romo J (2014). Shape outlier detection and visualization for functional data: The outliergram. *Biostatistics*, 15(4): 603–619.

Baladandayuthapani V, Mallick BK, Hong MY, Lupton JR, Turner ND, Carroll RJ (2008). Bayesian hierarchical spatially correlated functional data analysis with application to colon carcinogenesis. *Biometrics*, 64(1): 64–73.

Bhattacharya A, Dunson DB (2011). Sparse Bayesian infinite factor models. *Biometrika*, 98(2): 291–306.

Campos E, Scheffler AW, Telesca D, Sugar C, DiStefano C, Jeste S, et al. (2022). Multilevel hybrid principal component analysis for region-referenced functional EEG data. *Statistics in Medicine*, 41(19): 3737–3757.

Cardot H (2007). Conditional functional principal component analysis. *Scandinavian Journal of Statistics*, 34(2): 317–335.

Chen K, Müller HG (2012). Modelling repeated functional observations. *Journal of the American Statistical Association*, 107(500): 1599–1609.

Chiang AKI, Rennie CJ, Robinson PA, van Albada SJ, Kerr CC (2011). Age trends and sex differences of alpha rhythms including split alpha peaks. *Clinical Neurophysiology*, 122(8): 1505–1517.

Cragg L, Kovacevic N, McIntosh AR, Poulsen C, Martinu K, Leonard G, et al. (2011). Maturation of EEG power spectra in early adolescence: A longitudinal study. *Developmental Science*, 14(5): 935–943.

Crainiceanu CM, Ruppert D, Carroll RJ, Joshi A, Goodner B (2007). Spatially adaptive Bayesian penalized splines with heteroscedastic errors. *Journal of Computational and Graphical Statistics*, 16(2): 265–288.

Crainiceanu CM, Staicu AM, Di CZ (2009). Generalized multilevel functional regression. *Journal of the American Statistical Association*, 104(488): 1550–1561.

Di CZ, Crainiceanu CM, Caffo BS, Punjabi NM (2009). Multilevel functional principal component analysis. *The Annals of Applied Statistics*, 3(1): 458–488.

Dickinson A, DiStefano C, Şentürk D, Jeste SS (2018). Peak alpha frequency is a neural marker of cognitive function across the autism spectrum. *European Journal of Neuroscience*, 47(6): 643–651.

Dustman RE, E SD, Emmerson RY (1999). Life-span changes in EEG spectral amplitude, amplitude variability and mean frequency. *Clinical Neurophysiology*, 110(8): 1399–1409.

Edgar J, Heiken K, Chen Y, Herrington J (2015). Resting-state alpha in autism spectrum disorder and alpha associations with thalamic volume. *Journal of Autism and Developmental Disorders*, 45(3): 795–804.

Genton MG, Johnson C, Potter K, Stenchikov G, Sun Y (2014). Surface boxplots. *Stat*, 3(1): 1–11.

Gijbels I, Nagy S (2017). On a general definition of depth for functional data. *Statistical Science*, 32(4): 630–639.

Greven S, Crainiceanu CM, Caffo BS, Reich D (2010). Longitudinal functional principal component analysis. *Electronic Journal of Statistics*, 4: 1022–1054.

Hasenstab K, Scheffler A, Telesca D, Sugar CA, Jeste S, DiStefano C, et al. (2017). A multidimensional functional principal component analysis of EEG data. *Biometrics*, 73(3): 999–1009.

James GM, Hastie TJ, Sugar CA (2000). Principal component models for sparse functional data. *Biometrika*, 87(3): 587–602.

Krivobokova T, Kneib T, Claeskens G (2010). Simultaneous confidence bands for penalized spline estimators. *Journal of the American Statistical Association*, 105(490): 852–863.

Li Q, Shamshoian J, Şentürk D, Sugar C, Jeste S, DiStefano C, et al. (2020). Region-referenced spectral power dynamics of EEG signals: A hierarchical modeling approach. *Annals of Applied Statistics*, 14(4): 2053–2068.

López-Pintado S, Qian K (2020). A depth-based global envelope test for comparing two groups of functions with applications to biomedical data. *Statistics in Medicine*, 40(7): 1639–1652.

López-Pintado S, Romo J (2009). On the concept of depth for functional data. *Journal of the*

American Statistical Association, 104(486): 718–734.

López-Pintado S, Wrobel J (2017). Robust non-parametric tests for imaging data based on data depth. *Stat*, 6(1): 405–419.

Miskovic V, Ma X, Chou CA, Fan M, Owens M, Sayama H, et al. (2015). Developmental change in spontaneous electrocortical activity and network organization from early to late childhood. *Neuroimage*, 118: 237–247.

Montagna S, Tokdar ST, Neelon B, Dunson DB (2012). Bayesian latent factor regression for functional and longitudinal data. *Biometrics*, 68(4): 1064–1073.

Ramsay JO, Silverman BW (2005). *Functional Data Analysis*. Springer, New York, New York.

Scheffler A, Telesca D, Li Q, Sugar CA, Distefano C, Jeste S, et al. (2020). Hybrid principal component analysis for region-referenced longitudinal functional EEG data. *Biostatistics*, 21(1): 139–157.

Scheffler AW, Dickinson A, DiStefano C, Jeste SS, Şentürk D (2022). Covariate-adjusted hybrid principal components analysis for region-referenced functional EEG data. *Statistics and Its Interface*, 15(2): 209–223.

Scheffler AW, Telesca D, Sugar CA, Jeste SS, Dickinson A, DiStefano C, et al. (2019). Covariate-adjusted region-referenced generalized functional linear model for EEG data. *Statistics in Medicine*, 38(30): 5587–5602.

Shamshoian J, Şentürk D, Telesca D (2022). Bayesian analysis of longitudinal and multidimensional functional data. *Biostatistics*, 23(2): 558–573.

Somsen RJ, van't Klooster BJ, van der Molen MW, van Leeuwen HM, Licht R (1997). Growth spurs in brain maturation during middle childhood as indexed by EEG power spectra. *Biological Psychology*, 44(3): 187–209.

Staicu AM, Crainiceanu CM, Carroll RJ (2010). Fast methods for spatially correlated multilevel functional data. *Biostatistics*, 11(2): 177–194.

Stroganova TA, Orekhova EV, Posikera IN (1999). EEG alpha rhythm in infants. *Clinical Neurophysiology*, 110(6): 997–1012.

Suarez A, Ghosal S (2017). Bayesian estimation of principal components for functional data. *Bayesian Analysis*, 12(2): 311–333.

Sun Y, Genton MG (2012). Functional boxplots. *Journal of Computational and Graphical Statistics*, 20(2): 316–334.

Sun Y, Genton MG, Nychka DW (2012). Exact fast computation of band depth for large functional datasets: How quickly can one million curves be ranked? *Stat*, 1(1): 68–74.

Wang JL, Chiou JM, Müller HG (2016). Functional data analysis. *Annual Review of Statistics and its Application*, 3: 257–295.

Yao F, Müller HG, Wang JL (2012). Functional data analysis for sparse longitudinal data. *Journal of the American Statistical Association*, 100(470): 577–590.

Zipunnikov V, Caffo B, Yousem DM, Davatzikos C, Schwartz BS, Crainiceanu C (2011). Multilevel functional principal component analysis for high-dimensional data. *Journal of Computational and Graphical Statistics*, 20(4): 852–873.

Zuo Y, Serfling R (2000). General notions of statistical depth function. *The Annals of Statistics*, 28(2): 461–482.